Modelling and dynamic analysis of a synchropter

Bertolani, Giulia; de Angelis, Emanuele L.; Giulietti, Fabrizio; Pavel, Marilena D.

DOI
10.1016/j.ast.2024.109664

Publication date
2024

Document Version
Final published version

Published in
Aerospace Science and Technology

Aerospace Science and Technology 155 (2024) 109664

Contents lists available at ScienceDirect

Aerospace Science and Technology

journal homepage: www.elsevier.com/locate/aescte

Modelling and dynamic analysis of a synchropter

Giulia Bertolani [a,*], Emanuele L. de Angelis [a], Fabrizio Giulietti [a], Marilena D. Pavel [b]

[a] University of Bologna, Department of Industrial Engineering, Forlì, 47121, Italy
[b] TU Delft, Department of Control and Simulation, Delft, 2600, the Netherlands

ARTICLE INFO

Communicated by Antonio Filippone

Keywords:
Intermeshing rotors
Synchropter
Stability and dynamic analysis

ABSTRACT

This paper addresses the flight dynamics modelling, trim, and dynamic analysis of an intermeshing-rotor helicopter, indicated as synchropter. This configuration has gained a great interest for its suitability within heavy load lifting and transportation in extreme high temperature and altitude, and other harsh environments. The paper presents some relevant features related to synchropter's flight dynamics modelling of the interference between its two tilted main rotors. Trim results show the advantage of the synchropter in forward flight where the yawing moment is naturally balanced at almost all speeds and no lateral-directional compensation is needed. The synchropter's dynamic stability shows similarity to a conventional helicopter in the longitudinal phugoid. However, in the lateral phugoid, the synchropter is unstable at all flying speeds and therefore its vertical fin needs to be carefully designed.

Notations

List of Symbols

a_0	Rotor coning angle	rad
a_1	Longitudinal TPP deflection angle in rotor-hub system	rad
A_1	Lateral cyclic angle	rad
b_1	Lateral TPP deflection angle in rotor-hub system	rad
B_1	Longitudinal cyclic angle	rad
$\tilde{D}$	Damping matrix	
$\tilde{f}$	Forcing function	
$\boldsymbol{F} = [X\ Y\ Z]^T$	Force vector	N
g	Gravity acceleration	m/s^2
$\boldsymbol{I}$	Inertia tensor	kg/m^2
$\tilde{K}$	Stiffness matrix	
m	Mass	kg
$\boldsymbol{M} = [L\ M\ N]^T$	Moment vector	Nm
R	Rotor radius	m
$\boldsymbol{V} = [u\ v\ w]^T$	Velocity vector	m/s
w_H	Vertical speed in Hub-Body frame	m/s

Greek symbols

α	Angular opening	rad
β	Blade flapping	rad
ϕ, θ, ψ	Roll, pitch, yaw euler angles	rad
ρ	Density	kg/m^3
λ	Inflow ratio	
λ_0	Uniform inflow ratio	
Γ	Synchropter tilt angle	rad
Θ_0	Blade collective	rad
Θ_{ped}	Yaw command	rad
χ	Direction indicator	
$\boldsymbol{\Omega} = [p\ q\ r]^T$	Angular velocity vector	rad/s
Ω	Rotor angular velocity	rad/s
ζ	Azimuth blade angle	rad

* Corresponding author at: University of Bologna, Department of Industrial Engineering, Forlì, 47121, Italy.
E-mail addresses: giulia.bertolani2@unibo.it (G. Bertolani), emanuele.deangelis4@unibo.it (E.L. de Angelis), fabrizio.giulietti@unibo.it (F. Giulietti), m.d.pavel@tudelft.nl (M.D. Pavel).

https://doi.org/10.1016/j.ast.2024.109664
Received 4 March 2024; Received in revised form 10 October 2024; Accepted 10 October 2024
Available online 16 October 2024

Subscripts and superscripts

^{a}	Aerodynamical
cl	Clockwise
ccl	Counter-clockwise
e	Equilibrium condition
^{e}	External
FU	Fuselage
^{g}	Gravitational
HS	Horizontal stabilizer
MR	Main rotors
VS	Vertical stabilizer

Acronyms

BL	Buttline
NED	North East Down
RF	Reference Frame
STA	Stationline
$TPPV$	Tip Path Plane
UAV	Unmanned Aerial Vehicle
WL	Waterline

1. Introduction

A particular helicopter configuration, which represents an interesting solution for heavy load transportation for Urban Smart Delivery applications, is the intermeshing-rotor helicopter, or synchropter. Such configuration is a rotary-wing aircraft with a set of two counter-rotating rotors turning in opposite directions. Rotors are assembled with a slight angle each others, in a transversely symmetrical manner, allowing the blades to intermesh without colliding.

The first synchropter was developed by Anton Flettner [1] during second world war. In the 1980's and 1990's Kaman Aircraft successfully developed what today is known as K-MAX® intermeshing-rotor helicopter.

The synchropter has two counter-rotating intermeshing rotors. With respect to the classic helicopter configuration of one rotor and one tailrotor system, the synchropter allows the yaw to be accomplished through varying torque, which is performed by increasing collective pitch on one of the rotors. This allows the yaw-axis torque balance without the need for a tail-rotor system.

With respect to the conventional helicopter configuration, the synchropter presents the following benefits: 1) the symmetrical configuration allows for a more compact helicopter size and a more suitable payload arrangement; 2) the absence of a tail-rotor system allows for a 15% total power savings for the hovering condition [2]; 3) the intermeshing-rotor layout makes the helicopter have good stability and high lift coefficient, which allows it suitable for transportation in extreme high temperature, high altitude and other harsh environments [3]. However, spreading the total thrust in two smaller rotors decreases the overall aerodynamic efficiency while increasing the complexity of mechanical design [4,5].

Synchropter literature is mainly related to the Kaman K-MAX® aircraft, for which performance analysis, structural investigation, aerodynamic design and control system definition have been addressed [6–10] whereas other works are related to system identification of small-scale platform projects [3,11–14]. Recently, intermeshing-rotors configurations started becoming attractive also among rotary-wing unmanned platforms. The unmanned project that has received most attention is the Broad-area Unmanned Responsive Resupply Operations (BURRO), based on the Kaman K-MAX® platform [6–8]. Mansur et al. [6] in their work present a control law improvement for the unmanned K-Max®. In this paper, the authors also outline the development of identified-state space models from flight data. Also in paper [7] the authors propose a development of flight control system for unmanned K-Max®, based on identified flight test data, as well as Coulbourne et al. in [8] and McGonagle [9]. The work of Saribay [10] focuses on the analysis and design of transmission system. With regards to small-scale platforms, Barth et al. [11,12] present in their works the design and analysis of the performance of a small scale intermeshing rotors system, with special attention to high altitude performance. In the paper of Wei et al. [3], the authors study the influence of the lateral shaft tilt angle on rotor thrust, power required and rotor clearance through the use of a small-scale intermeshing rotors test platform. A recent paper from Zappek and Yavrucuk [13] presents the models and methods to convert a small-scale synchropter with electric propulsion to one with hydrogen hybrid power source. Their results illustrate requirements for the propulsive system. Wartmann et al. [14] using system identification for the superARTIS DLR-operated unmanned syncopter helicopter, discusses the eigenvalues and modes obtained for the hover case. The results are dependent on the identification method used. In the optimized Predictor-Based Subspace Identification method (PBSIDopt) provides an unstable phugoid and a stable dutch roll mode. In the frequency response (FR) method the phugoid mode is separated into roll and pitch and the longitudinal and heave dynamics are not coupled with the lateral-directional dynamics.

In the literature of speciality, there are various works addressing the issue of modelling of the aerodynamic interference effects on intermeshing rotors [2,15,16]. These are mainly focused on numerical simulations of the intermeshing system [2], showing experimental results [16] or presenting numerical investigation of the aerodynamic interaction of rotorcraft-to-rotorcraft interference during shipboard operations [17]. There are also many works addressing the modelling of the aerodynamics rotors interference, considering two rotors that can be from partially (as in synchropter or tandem helicopters configurations) to totally overlapped (as in coaxial helicopters configurations). From an aerodynamic point of view, Leishman [4,18] gives an overview of the interference modelling for many helicopter configurations. With special regards to tandem configuration, Bramwell reports the longitudinal [19] and lateral [20] stability analysis, while Stepniewski [21] discusses extensively this configuration in its work, as well as [22], in which the authors discuss trims, stability, controllability and qualities of tandem rotor helicopter. However, to the best of the authors' knowledge, most of the current research related to the synchropter aircraft focuses only on performances analysis based on experimental validation [2,16] without providing a generalized theoretical framework for addressing preliminary design, optimal sizing and control system design. Moreover, the few existing models presented in the literature are obtained from Kaman K-MAX® (and other small unmanned platforms) by means of systems identification algorithms [6,14].

Yet, the literature currently lacks of an analytical framework for precisely defining synchropter flight dynamics behaviour and stability problems, as well as investigation of the dynamic stability characteristics compared to a conventional helicopter. This study seeks to address this gap by providing an initial framework for dynamic analysis.

The scope of the present paper is to derive a flight dynamic analytical framework with the aim to analyze synchropter trim and stability by highlighting longitudinal and lateral-directional dynamic features. The contributions of the present paper are multifold: 1) reference model is provided and discussed, which includes the aerodynamic effects related to the intermeshing configuration; 2) state and control variables are characterized in forward flight condition for different values of speed and trend discussion; 3) an extensive discussion is provided with respect to dynamic properties for different values of advance ratio which includes an analysis of most relevant stability and control derivatives; 4) a comparison is provided between results obtained with the proposed modelling approach and experimental data, obtained for a small scale unmanned rotorcraft given in [14].

The rest of the paper is structured as follows. Section 2 addresses the nonlinear model. Results of the trim comparison with the well-documented BO105 helicopter are detailed in Section 3, whereas stability analysis is given in Section 4. Then, Section 5 presents a comparison for hovering dynamic stability between identified data for a synchropter UAV and the presented model. Final conclusions will end this paper.

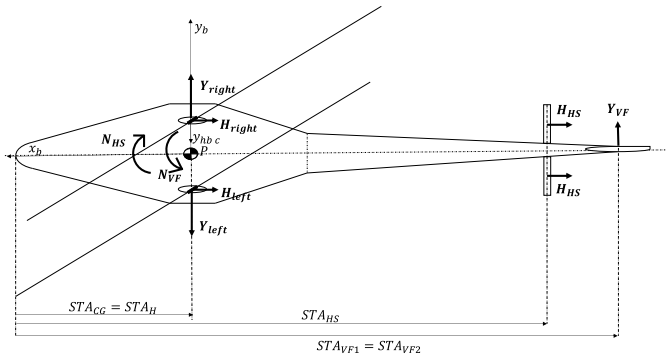

(a) Synchropter XY view

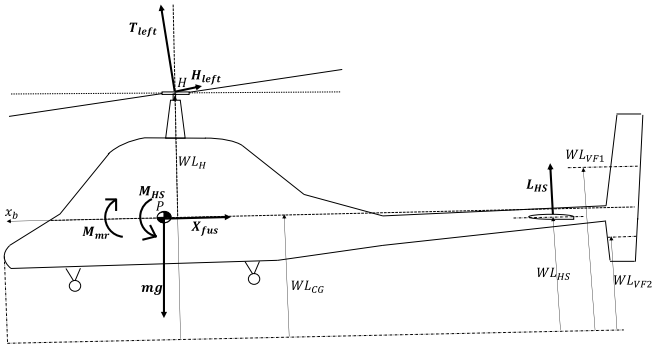

(b) Synchropter XZ view

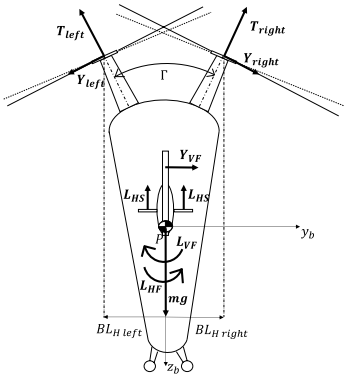

(c) Synchropter YZ view

Fig. 1. Synchropter views.

2. Mathematical modelling

The synchropter nonlinear mathematical model has 14 degrees of freedom (dof), including 6 dof of the body dynamics, a medium complexity of rotor dynamics (3 dof for the second order flapping dynamics for each rotor) and a dynamic inflow (2 dof for both rotors) that is assumed to be uniform, based on Pitt-Peters equations [23]. The mathematical model is based on the Talbot's [24] conventional one rotor-tail rotor helicopter configuration that has been adapted to represent the intermeshing rotor helicopter. In particular, the model of the main rotor for the counter-clockwise rotor has been developed based on [24] and briefly described in section 2.2.1. The same model, adapted for the clockwise rotor, has been applied for the other main rotor and considering the absence of the tail rotor in the synchropter, it has not been modelled. Interference effects between the two main rotors have been accounted as shown in 2.2.2. The two intermeshing rotors are tilted in this paper by the same angle as in the Kaman K-MAX® configuration, i.e. the intermeshing angle of the rotors is $\Gamma = 25\,\text{deg}$, see Fig. 1c. This Γ angle refers to lateral shaft tilting of the two main rotors on the YZ plane. The aerodynamic interference effects related to the intermeshing rotors are also given. The fuselage is considered as a flat plate area being modelled as in Padfield [25]. Blades are assumed rigid with integral form dependent on control actions, vehicle kinematics and flapping equations. The rotation matrices from the body-fixed frame $\mathbb{F}_b$ to the rotor hub frame $\mathbb{F}_{hbcc}$ for the counter-clockwise and clockwise rotor are given by, respectively:

$$\mathbb{T}_{hbcc} = \begin{bmatrix} 1 & 0 & 0 \\ 0 & \cos\frac{\Gamma}{2} & -\sin\frac{\Gamma}{2} \\ 0 & \sin\frac{\Gamma}{2} & \cos\frac{\Gamma}{2} \end{bmatrix} \qquad \mathbb{T}_{hbc} = \begin{bmatrix} 1 & 0 & 0 \\ 0 & -\cos\frac{\Gamma}{2} & -\sin\frac{\Gamma}{2} \\ 0 & -\sin\frac{\Gamma}{2} & \cos\frac{\Gamma}{2} \end{bmatrix} \tag{1}$$

2.1. Equations of motion

Synchropter aircraft dynamics is described by Newton-Euler equations of motion projected in the body frame $\mathbb{F}_b$. Fig. 1a, 1b, 1c represents the main forces and moments acting on the synchropter. Specifically:

$$\dot{\boldsymbol{V}} = -\boldsymbol{\Omega} \times \boldsymbol{V} + \boldsymbol{F}^{(e)}/m \qquad \dot{\boldsymbol{\Omega}} = \boldsymbol{I}^{-1}[-\boldsymbol{\Omega} \times (\boldsymbol{I}\boldsymbol{\Omega}) + \boldsymbol{M}^{(e)}] \tag{2}$$

where m is the aircraft mass, $\boldsymbol{V} = [u, v, w]^T$ is the linear velocity vector, $\boldsymbol{\Omega} = [p, q, r]^T$ is the angular velocity vector, and $\boldsymbol{I}$ is the inertia tensor. $\boldsymbol{F}^{(e)}$ and $\boldsymbol{M}^{(e)}$ are the external forces and moments, respectively.

$$\begin{bmatrix} \dot{\phi} \\ \dot{\theta} \\ \dot{\psi} \end{bmatrix} = \begin{bmatrix} 1 & \sin\phi\tan\theta & \cos\phi\tan\theta \\ 0 & \cos\phi & -\sin\phi \\ 0 & \sin\phi/\cos\theta & \cos\phi/\cos\theta \end{bmatrix} \boldsymbol{\Omega} \tag{3}$$

Rigid-body kinematics is given by $\dot{\boldsymbol{X}} = \mathbb{T}_{be}^T \boldsymbol{V}$, provided $\boldsymbol{X}$ represents the position in the Earth-fixed reference frame and $\mathbb{T}_{be}(\psi, \theta, \phi)$ being the Earth-fixed to Body axes rotational matrix obtained by means of a $3-2-1$ rotation sequence.

2.2. Forces and moments

The external force vector contains the aerodynamic $\boldsymbol{F}^{(a)}$ and gravity $\boldsymbol{F}^{(g)}$ contributions, whereas total moment vector includes mainly the aerodynamic $\boldsymbol{M}^{(a)}$ effect. Gravity force vector is given by:

$$\boldsymbol{F}^{(g)} = \mathbb{T}_{be} \begin{bmatrix} 0 & 0 & mg \end{bmatrix}^T \tag{4}$$

provided that $\mathbb{T}_{be}$ is being the rotation matrix from Earth-fixed to Body frame and g the gravity constant. Aerodynamic effects are expressed as the sum of aircraft components contributions:

$$\boldsymbol{F}^{(a)} = \boldsymbol{F}^{(MR)} + \boldsymbol{F}^{(FUS)} + \boldsymbol{F}^{(VS)} + \boldsymbol{F}^{(HS)} \tag{5}$$

$$\boldsymbol{M}^{(a)} = \boldsymbol{M}^{(MR)} + \boldsymbol{M}^{(FUS)} + \boldsymbol{M}^{(VS)} + \boldsymbol{M}^{(HS)} \tag{6}$$

Looking at Fig. 1a, 1b, 1c one can see that the rotor is characterized by three forces: the thrust T, the horizontal force H and the lateral force Y. In the Figs. 1a, 1b, 1c these are showed for the left and right rotors. The empennages and fuselage forces and moments are also represented. In particular, horizontal and lift forces for horizontal stabilizer and lateral and lift forces for vertical stabilizers.

2.2.1. Main rotors model

The total aircraft thrust is generated by means of two intermeshing counter-rotating tilted rotors. The mathematical model for the single counter-clockwise (ccl) rotor is based on the single rotor Talbot's model [24]. To this aim, the following assumptions are made: 1) blades are considered to be rigid both in bending and torsion; 2) flapping angles are small, and the analysis follows the simple strip theory [4]; 3) the effects of aircraft motion on blade flapping are limited to those related to the angular accelerations $\dot{p}$ and $\dot{q}$, the angular rates p and q, and the normal acceleration component $\dot{w}$; 4) blade stall and radial flow are disregarded, as well as tip and root cut-out vortices; 5) high-speed compressibility issues and tip relief effects on advancing blades are not

accounted; 6) reverse flow region is ignored; 7) no dedicated flow description is provided for wake swirl and contraction; 8) rotor inflow is based on Pitt-Peters equations [23], in contrast to that one presented by Talbot, but only uniform inflow component is considered as follows. In the Pitt-Peters equation the terms λ_s and λ_c are set equal to zero, in order to account only for the uniform inflow component λ_0. In the hub-wind reference frame the equation is:

$$\left[\dot{\lambda}_0\ \dot{\lambda}_s\ \dot{\lambda}_c\right]^T = \boldsymbol{\Omega}\mathbb{M}^{-1}(-(\mathbb{L}_1\mathbb{L}_2)^{-1}\left[\lambda_0\ \lambda_s\ \lambda_c\right]^T + \boldsymbol{C}_{aero} \tag{7}$$

where the expressions for the matrices C_{aero}, $\mathbb{L}_1$, $\mathbb{L}_2$ and $\mathbb{M}$ are reported in [23]. 9) Main rotor blade flapping is approximated by the first harmonic terms with time-varying coefficients, that is $\beta(t) = a_0 - a_1\cos\zeta - b_1\sin\zeta$, where a_0 is the preset coning angle, ζ the blade azimuth and a_1, b_1 represents the longitudinal and lateral tilt of the tip-path plane. The vector $\boldsymbol{a} = \left[a_0\ a_1\ b_1\right]^T$ is the solution of equation (8):

$$\ddot{\tilde{\boldsymbol{a}}} + \tilde{D}\dot{\tilde{\boldsymbol{a}}} + \tilde{K}\tilde{\boldsymbol{a}} = \tilde{\tilde{\boldsymbol{f}}} \tag{8}$$

and expressions for $\tilde{D}$, $\tilde{K}$ and $\tilde{\boldsymbol{f}}$ are found in Appendix C of [24]. Since the synchropter has two counter-rotating main rotors, the model described above for a counter-clockwise (ccl) rotor has been adapted for the clockwise (cl) one in the following manner. Equations for the ccl rotor equations derived using a left-hand side coordinate system are applied to the cl by adopting a direction indicator χ in the lateral equations of motion, which value is equal to 1 when rotor is counter-clockwise and -1 otherwise [26]. Resulting equations are given as follows:

$$\begin{aligned} &\boldsymbol{V}_{cl} = \Pi_1\boldsymbol{V}_{ccl} \quad \boldsymbol{\Omega}_{cl} = \Pi_2\boldsymbol{\Omega}_{ccl} \quad \boldsymbol{F}_{cl} = \Pi_1\boldsymbol{F}_{ccl} \\ &\boldsymbol{M}_{cl} = \Pi_2\boldsymbol{M}_{ccl} \quad \boldsymbol{U}_{cl} = \Pi_1\boldsymbol{U}_{ccl} \end{aligned} \tag{9}$$

provided

$$\Pi_1 = \begin{bmatrix} 1 & 0 & 0 \\ 0 & \chi & 0 \\ 0 & 0 & 1 \end{bmatrix} \quad \Pi_2 = \begin{bmatrix} \chi & 0 & 0 \\ 0 & 1 & 0 \\ 0 & 0 & \chi \end{bmatrix} \tag{10}$$

and $\boldsymbol{U} = [\theta_0 \quad A_1 \quad B_1]$ respectively representing the collective, longitudinal and lateral cyclic controls.

2.2.2. Rotors interference

Aerodynamic interference effects, due to the partial overlapping between the two main rotors are taken into account according to the Leishman's model for coaxial rotor model, Refs. [4,18]. In Ref. [18], a simple steady momentum theory is adapted to represent the inflow of coaxial configurations, under the assumption that the induced velocity changes instantaneously across the rotor disk. Since rotors are not coaxial, in the proposed synchropter configuration, the rotor interference induced power factor k is scaled for thrust computation, accordingly to the actual overlapping fraction of the disk area. Such procedure has been presented by Leishman in his book [4] for tandem rotors configuration where the scaling factor is ratio between the overlapping area A_{OV} and the total rotor area.

The overlapping area between the two rotors, A_{OV}, is derived by projecting the radius of a single tilted rotor from XY-plane of the Hub-Body to the un-tilted XZ-plane of the body axis system and considering the length of overlapping distance. The area is geometrically estimated, whereas seen from the top it mainly appears as an intersection of two circular sectors. Then equivalent radius is estimated and the ratio between the areas is found. According to Fig. 2, equations allowing for the estimation of the overlapping area are:

$$A_{OV} = 2A_{CS} - A_R \tag{11}$$

where $A_{CS} = \frac{R_{PRO}^2\alpha}{2}$ is the area of the circular sector with projected radius $R_{PRO} = R\cos(\Gamma/2)$ and angular opening $\alpha = 2\cos^{-1}(d/R_{PRO})$; $A_R = d\,R_{PRO}\sin(\alpha/2)$ is the area of the rhombus with diagonals d and $2\,R_{PRO}\sin(\alpha/2)$.

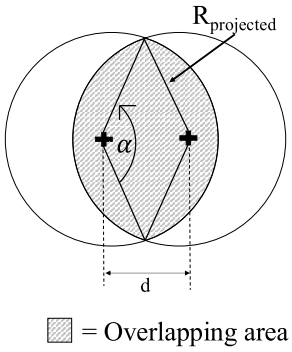

Fig. 2. Overlapping area geometry.

Once the overlapping area is obtained, it is utilized to evaluate the value of the interference induced power factor k based on [4]:

$$k = 1 + (\sqrt{2} - 1)\frac{A_{OV}}{A} \tag{12}$$

where A is the rotor area.

Recalling the hypotheses for the mathematical model of main rotors given in Section 2.2.1, the complexity of the analysis is increased by the aerodynamic interference between the two rotors. This interference introduces additional challenges that warrant further investigation, which could be more accurately addressed through the use of advanced Computational Fluid Dynamics (CFD) simulations and/or dedicated experimental testing. Considering the level of aerodynamic modelling utilized, the method for accounting the interference appears reasonable.

2.2.3. Fuselage and empennages model

Throughout the flight envelope, the fuselage aerodynamic model produces forces and moments as a function of angle of attack and sideslip angle. Effects are taken into consideration in performance and stability analysis for forward speeds. Details on the procedure to calculate forces and moments equations are available in Padfield [25].

Vertical fin and horizontal tail are considered as lift and drag producers and are approximated for all angles of attack and sideslip. Equations are given in detail in Talbot [24].

The interaction between the rotors and the fuselage and tail planes is included in the same way as in [24]. It consists in the introduction of an averaged effect of rotor downwash in angles of attack, sideslip angles and dynamic pressures of fuselage, vertical fin and horizontal plane.

3. Trim analysis

The nonlinear aircraft model described in Section 2, characterized by mass and inertia properties, and geometric and aerodynamic data listed in Table A.3 in Appendix A, is implemented in the Matlab/Simulink environment. The differential equations are solved by the eight-order Dormand–Prince method [27] with a frequency of 1000 Hz. The synchropter model is then numerically trimmed in level flight in standard atmospheric conditions. The range of considered forward speed values is from 0 km/h to 200 km/h. To provide an accurate and direct comparison of the outcomes, the well-know classical helicopter BolkoW BO105 [25] was selected as baseline model for the implementation of the analytical framework of the synchropter. The Bo105 parameters have been adapted to represent a synchropter configuration with two counter-rotating tilted main rotors and no tail rotor as follows: a) synchropter main rotor radius is kept equal to BO105 one, but the number of blades for each rotor has been halved. In such a way the synchropter has two counter-rotating main rotors with the same radius and area of the BO105 but the total number of blades is still 4 (2 + 2); b) the aerodynamic parameters of the fuselage and tail surfaces of the synchropter are exactly the same of the BO105; c) the moments of inertia of synchropter have been calculated starting from those of BO105 reported

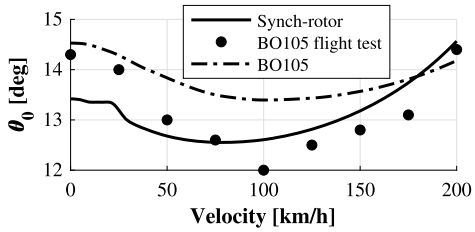

Fig. 3. Trim results: main rotor collective.

in [25] as follows. The helicopter is schematize considering the fuselage, the main rotor hub, the tail boom and the vertical and horizontal planes. These parts are approximated as an ellipsoid for the fuselage, as cylinders the rotor hub and the tail boom, as parallelepiped the vertical and horizontal planes. For each part the weight has been evaluated following Prouty formula [28]. The moments of inertia of each part are calculated with well-known formulas. The synchropter moments of inertia are evaluated with the same procedure but adding one main rotor hub in the correct position and recalculating the weights. Results show that synchropter rotors result in an approximated 30% increase in I_{xx} moment of inertia with respect to BO105, a 2% on I_{yy} and -2% I_{zz}. These values are reported in Appendix A. The yaw motion of the synchropter is controlled by a mix of differential longitudinal cyclic B_1 and differential main rotor collective θ_0. This means that the yaw axis is controlled by:

$$\theta_{ped} = \frac{\theta_0^l - \theta_0^r}{2} + \frac{B_1^l - B_1^r}{2}$$

where θ_0^l and θ_0^r are the actual values of the left and right rotors collectives, while B_1^l and B_1^r are the longitudinal cyclic of left and right rotor respectively. The global collective is then: $\theta_0 = \frac{\theta_0^l + \theta_0^r}{2}$ and lateral and longitudinal axes are controlled as: $A_1 = A_1^l = -A_1^r$, $B_1 = \frac{B_1^l + B_1^r}{2}$.

Figs. 4-8 show the trim results of the synchropter model as compared to the BO105 helicopter, whose trim data are taken from Ref. [29]. The data for BO105 helicopter are both flight test data and simulator data. The BO105 simulator data are produced using the same mathematical model as described in section 2 in its initial version intended for a conventional one main-one tail rotor helicopter.

An interesting result from the trim procedure is the little difference in collective required by the two rotorcraft, as depicted in Fig. 3. For the synchropter, the required collective is lower than BO105 for speeds up to bucket speed. This is due to the presence of two main sources of lift, so that the collective required to sustain the vehicle in flight is reduced. However, the reduction in synchropter θ_0 is limited with respect to BO105 helicopter. Since for synchropter the number of blades per rotor is halved compared to BO105 main rotor, this allows to double the total disk area, while halving the solidity of a single synchropter rotor (synchropter solidity is 0.035, whereas BO105 solidity is 0.07). The disk area is kept as a constant, so the synchropter has a reduced disk loading, even if there is around 3% thrust loss for each rotor due to the lateral tilt angle $\Gamma = 25$ deg. Hence, the $\frac{C_T}{\sigma}$ is much the same between synchropter and BO105, so the θ_0 of synchropter is slightly lower.

Another consequence of having two intermeshing rotors is the difference between the lateral cyclic required. For the synchropter configuration, almost zero lateral cyclic is demanded in trim, due to the fact that the two tilted rotors flap in opposite directions. However, a significant amount of lateral cyclic is needed in a traditional helicopter like the BO105 to trim it, see in Fig. 5. In a classic helicopter, the blade incidence at the back of the rotor disk lowers as the helicopter enters forward flight due to the skewing backward of the rotor wake. The helicopter rolls to the starboard side as a result of this (for a counterclockwise rotor when seen from above). Hence, a lateral cyclic command needs to be given to mitigate this effect.

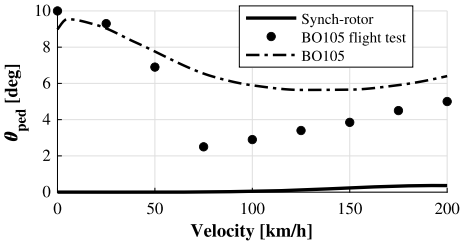

Fig. 4. Trim results: tail rotor collective.

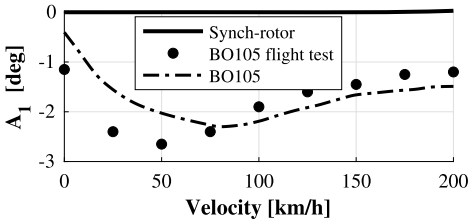

Fig. 5. Trim results: lateral cyclic.

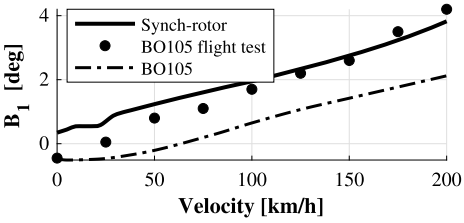

Fig. 6. Trim results: longitudinal cyclic.

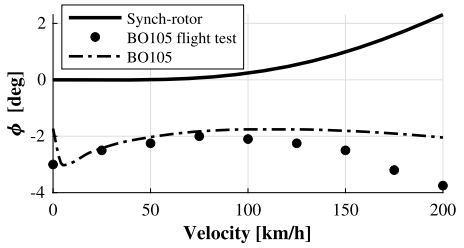

Fig. 7. Trim results: roll angle.

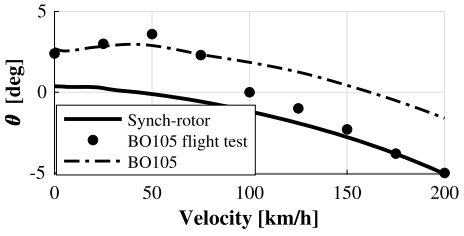

Fig. 8. Trim results: pitch angle.

Regarding the bank angle ϕ, again, the absence of the tail rotor results in a significant reduction of this angle. Indeed, without tail rotor, the side force is reduced and so is the fuselage angle, as depicted in Fig. 7.

On the longitudinal axis the difference between the longitudinal cyclic on the two configurations is negligible, see Fig. 6. In low speed flight, the pitch attitude is slightly different because of the absence of tail rotor, see Fig. 8, resulting in a small fuselage pitch angle required at the equilibrium. Accordingly to conventional helicopter behaviour, as speed increase, pitch angle becomes more negative.

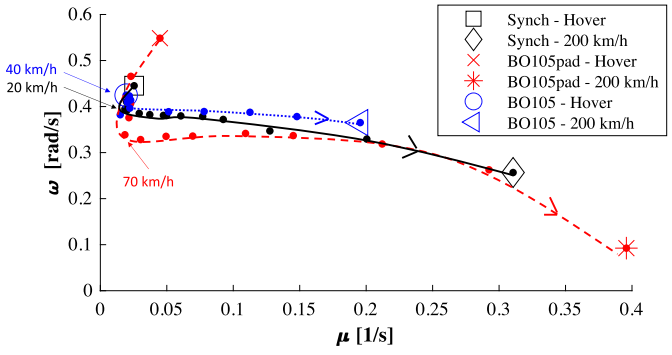

Fig. 9. Phugoid modes of the synchropter and BO105 helicopter. (For interpretation of the colours in the figure(s), the reader is referred to the web version of this article.)

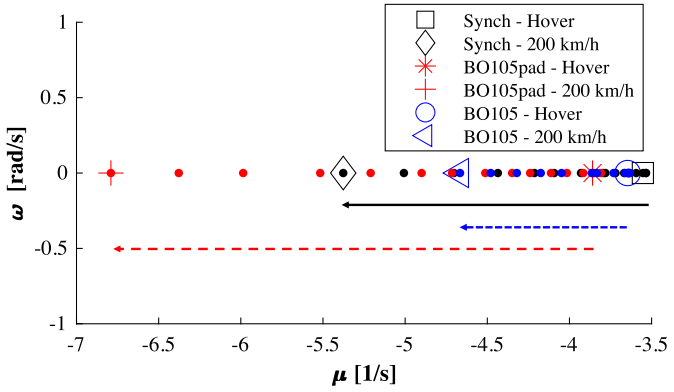

Fig. 10. Pitch subsidence modes of the synchropter and BO105 helicopter.

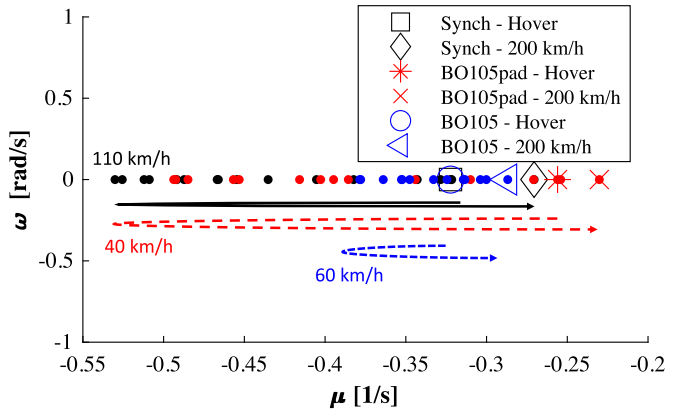

Fig. 11. Heave modes of the synchropter and BO105 helicopter.

Since the yawing moment is naturally balanced throughout practically the entire speed range, due to the presence of two counter-rotating rotors, no yaw command θ_{ped} is required. The θ_{ped} collective only assumes modestly positive values at speeds greater than 150 km/h, as depicted in Fig. 4. This result is due to the unsymmetrical aerodynamics that the fin produces at high speeds and requires slight compensation.

4. Dynamic stability analysis

In what follows the stability characteristics of the proposed synchropter configuration are compared with the same test cases of Section 3. Let $\boldsymbol{X} = \{u, w, q, \theta, v, p, \phi, r, \psi\}$ be the state vector and $\boldsymbol{U} = \{A_1, \theta_0, B_1, \theta_{ped}\}$ the control vector. Generally, the linearized model takes the form:

$$\dot{\boldsymbol{X}} = \boldsymbol{A}\boldsymbol{X} + \boldsymbol{B}\boldsymbol{U} \tag{13}$$

where the state and control matrices are obtained as:

$$\boldsymbol{A} = \left(\frac{\partial f}{\partial \boldsymbol{x}}\right)_{\boldsymbol{x}=\boldsymbol{x}_e} \qquad \boldsymbol{B} = \left(\frac{\partial f}{\partial \boldsymbol{u}}\right)_{\boldsymbol{x}=\boldsymbol{x}_e} \tag{14}$$

Aircraft stability derivatives in this paper are obtained numerically by applying central finite differential method. These are written in semi-normalized form, so that the forces derivatives are divided by aircraft mass and the moment derivatives by moment of inertia, in the same manner as described in Padfield [25]. The state and control matrices can be found at various trimmed conditions, so that the eigenvalues of the state matrix describe the natural modes of the motion at that flight condition. The form of the state and control matrices may be found in Appendix B. A dynamic stability analysis is carried out using this method from hover to 200 km/h.

Figs. 9, 11, 10 show the uncoupled longitudinal dynamics: the phugoid, the heave and the pitch subsidence of the intermeshing rotor helicopter (black line) as compared to the classic BO105 helicopter calculated using either the one rotor-one tailrotor helicopter model (dotted blue line) or the values presented in Padfield [25] (dashed red line).

Longitudinal dynamics do not exhibit any particular differences between the two configurations. As expected, phugoid is an unstable oscillatory mode. This is mainly due to the speed stability derivative M_u, that is positive for both synchropter and BO105 helicopter. The pitch damping derivative M_q is negative for all flight conditions from hover to forward flight, i.e. a pitch down moment is produced when the fuselage pitches up. This is due to the stiff rotors of both configurations which create a large moment around the rotor hub mainly due to the stiffness of the blades. When a perturbation in forward speed is experimented, the rotor will flap back and a pitch up moment will be experienced by the fuselage. As the rotor pitches up, the main rotors will provide a pitching down moment, being M_q negative.

Pitch subsidence mode is presented in Fig. 10 and shows that it is strongly influenced by M_q stability derivative. The M_q stability derivative shows the same trend for both the synchropter and the BO105 helicopter resulting thus in similar pitch subsidence mode for both helicopters.

The heave mode given in Fig. 11 is a stable damped mode dependent by Z_w stability derivative. The behaviour for the two configurations is similar, the main difference is that for the synchropter the more stable poles are situated at high velocity (around 110 km/h) while for the B0105 the more stable poles are at around 40 km/h.

Regarding longitudinal static stability, both systems demonstrate positive longitudinal static stability (statically stable), with $M_w > 0$ throughout the envelope.

Fig. 12 presents the longitudinal modes involvement on each axis. For example, one can see that heave is influenced by both w and w_0.

Figs. 13, 14, 15 present the uncoupled lateral dynamics characteristics of the synchropter: the roll subsidence, the spiral and lateral phugoid.

Looking at Fig. 13 one can see that the roll mode exhibits the same trend for both the synchropter and the BO105 helicopter. This is mainly because the roll damping stability derivative L_p behaves similarly in both configurations.

In order to better understand the influence of the different state variables on the modes, the lateral involvement of each lateral state variable in the synchropter lateral mode is given in Fig. 16. Lateral vector is composed by: $\boldsymbol{X}_{lat} = \{\dot{v}_0, v, \dot{v}, p\}$, where $v_0 = v + u_E\psi$ [25].

Synchropter spiral and lateral phugoid modes however show a different trend with respect to those of BO105 helicopter, as depicted in Fig. 14 and 15. Spiral mode is usually related to the yaw damping derivative N_r, whose trend is plotted in Fig. 17 as the forward speed increases. Looking at this figure one can see that, as the forward velocity increases, this derivative is greater for the synchropter as compared to the BO105 helicopter. Additionally, lateral mode involvement, see Fig. 16, shows

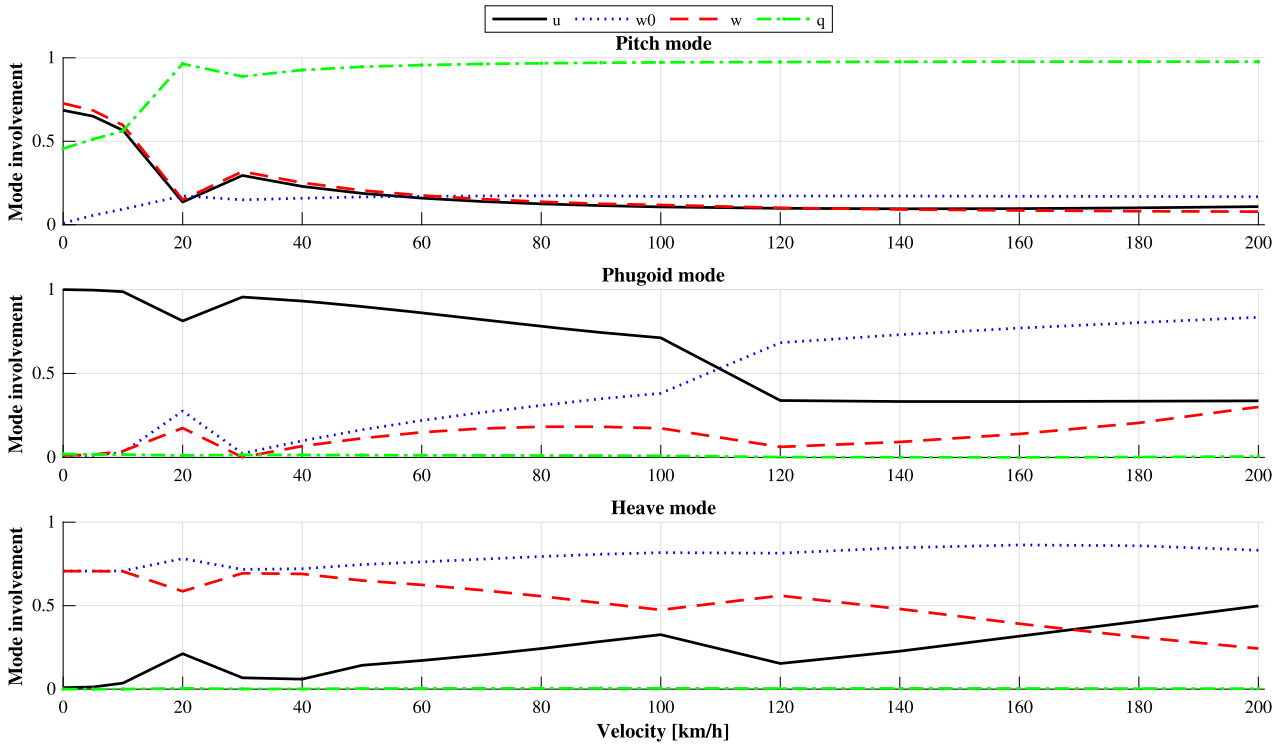

Fig. 12. Longitudinal modes: involvement of each mode.

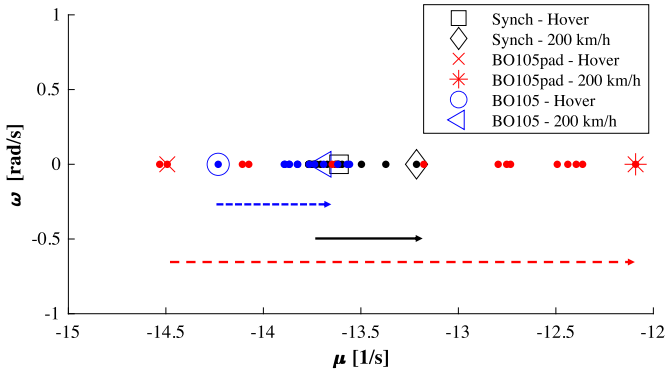

Fig. 13. Roll subsidence of the synchropter and BO105 helicopter.

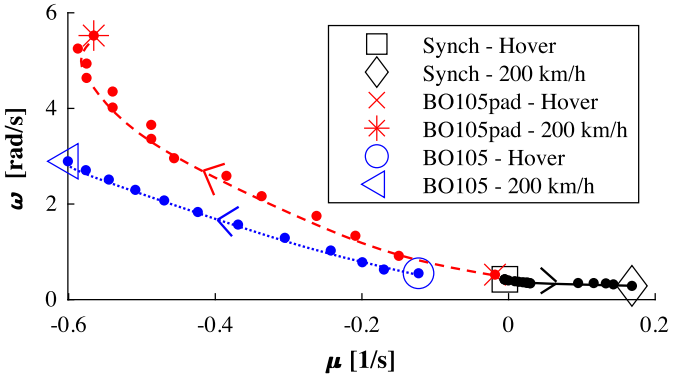

Fig. 15. Lateral phugoid of the synchropter and BO105 helicopter.

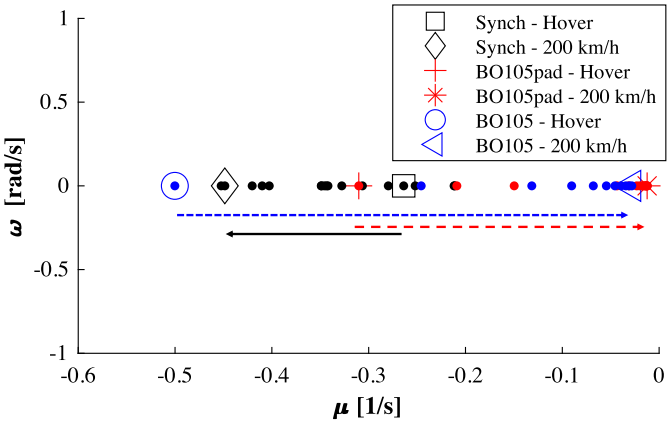

Fig. 14. Spiral modes of the synchropter and BO105 helicopter.

that spiral pole is influenced by the lateral speed, its derivative and by the yaw rate (that can be found in v_0 variable). Therefore, the N_v derivative is also influencing the spiral mode.

The weathercock stability derivative N_v is plotted in Fig. 18. In comparison to the conventional helicopter, for the synchropter this derivative is opposite in sign, being negative at all speeds. This has a strong influence on the lateral phugoid mode. In Fig. 15 it can be seen that lateral phugoid is an unstable oscillatory mode that is an opposite behaviour with respect to that of the BO105 helicopter. Following a sideslip disturbance, the fin and tail rotor generate a side force that aligns the helicopter's nose with the wind direction, producing a stabilizing effect. As a result, the helicopter's yawing moment after a sideslip disturbance is reduced. The lack of the tail rotor and the fact that the fin is not oriented in relation to the centreline of the fuselage make the weathercock derivative unstable for the synchropter configuration at all flying speeds and consequently also the lateral phugoid mode. This is also confirmed by the lateral modes involvement, see Fig. 16, wherein the v lateral speed almost entirely determines this synchropter mode.

Following on the N_v derivative, it is evident that the perturbation applied to the lateral speed v has a significant impact on the weathercock

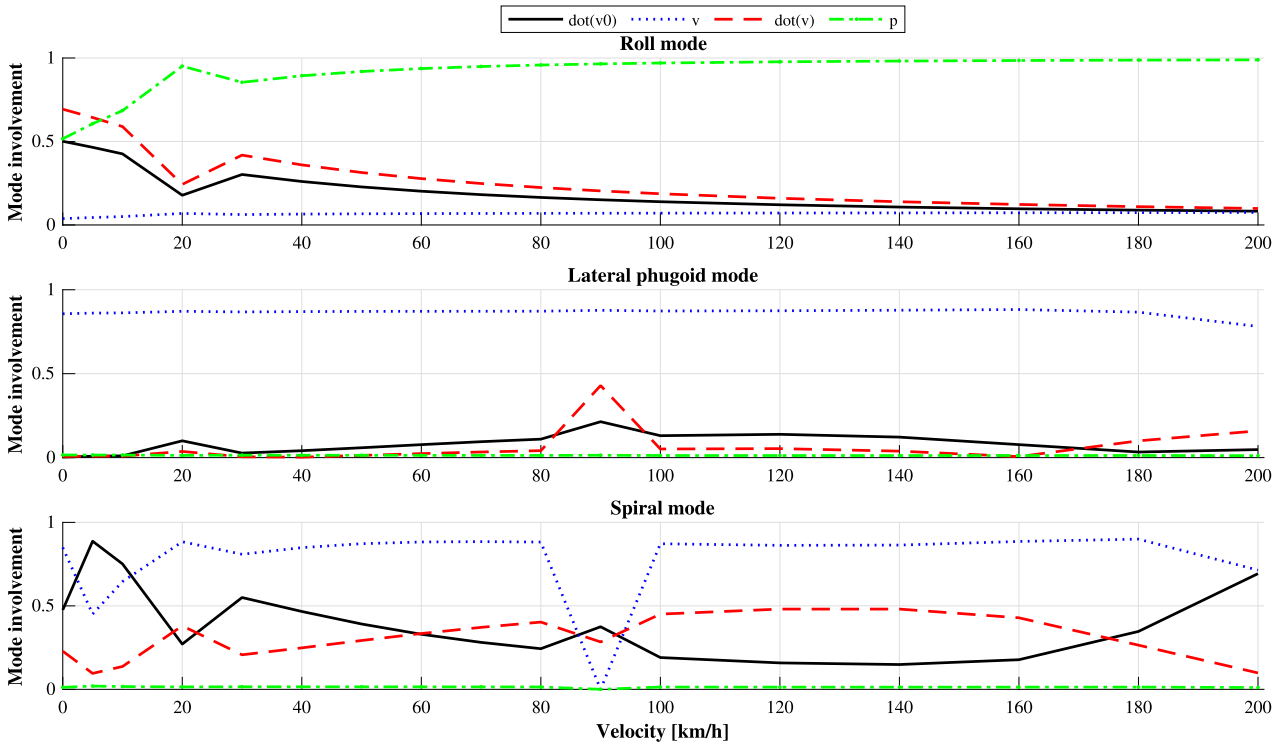

Fig. 16. Lateral modes: involvement of each mode.

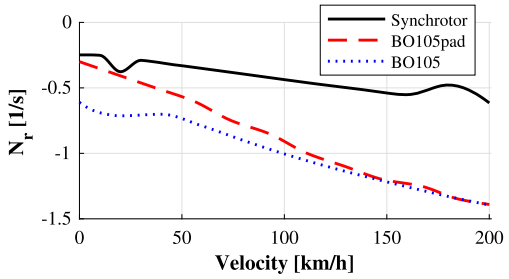

Fig. 17. Yaw damping derivative N_r.

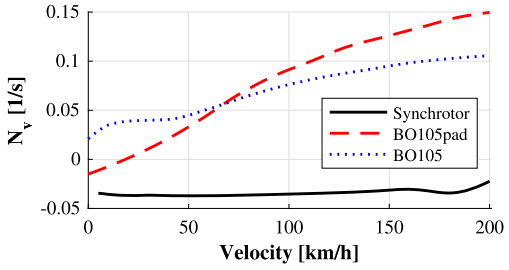

Fig. 18. Weathercock stability derivative N_v.

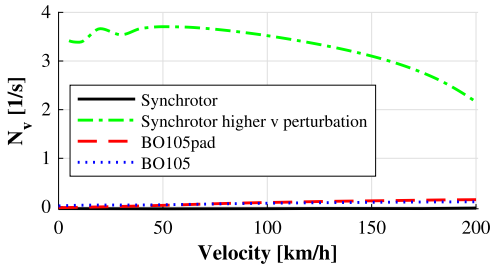

Fig. 19. Weathercock stability derivative N_v with higher v perturbation.

Table 1
Synchropter poles in hovering for a higher v perturbation.

Mode	Real part	Imaginary part
Roll subsidence	-13.622	0
Pitch subsidence	-3.5533	0
Heave	-0.32232	0
Longitudinal phugoid	0.02542	0.44525
Longitudinal phugoid	0.02542	-0.44525
Spiral	-0.26383	0
Lateral phugoid	-0.005061	0.4253
Lateral phugoid	-0.005061	-0.4253

stability derivative, that is reflected as a large change in side-slip angle. If a larger perturbation on v is applied when calculating N_v, the result is that this derivative becomes greater, see Fig. 19, and that the lateral phugoid mode becomes a stable oscillation. Poles of the synchropter in hovering with a larger perturbation on v are reported in Table 1.

5. Comparison of synchropter model with identified data from a scaled model

The proposed model has been further validated through a comparison with experimental data obtained from a UAV synchropter, specifically the SuperARTIS UAV. This comparison aims to highlight any discrepancies between the model predictions and the experimental data. The SuperARTIS UAV is a synchropter platform whose dynamic characteristics, including its poles, have been previously identified in [14]. To facilitate this comparison, modifications were made to the synchropter model, originally designed for a full-scale vehicle, in order to adapt it to the SuperARTIS UAV configuration. The parameters corresponding to the SuperARTIS UAV were incorporated into the model, and the detailed procedure for adapting the synchropter model to this UAV is outlined below. The synchropter data have been adapted in the following manner: 1) Weight of the superARTIS UAV is used as input for the synchropter

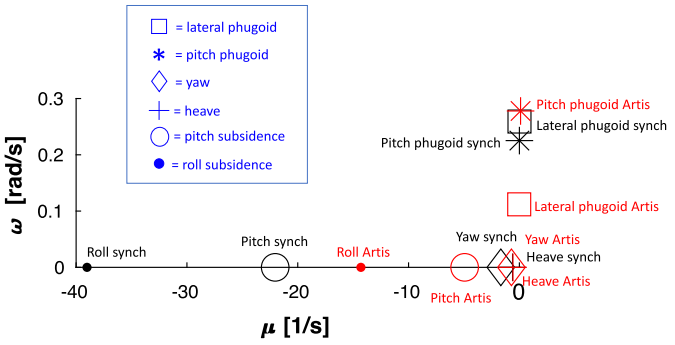

Fig. 20. Synchropter poles in hovering: comparison between scaled synchropter model and identified Superartis poles.

Table 2
Hovering poles of scaled synchropter and superARTIS UAV.

Mode	Synchropter Pole	superARTIS Pole
Roll subsidence	-39.017	-14.3
Pitch subsidence	-22.036	-4.94
Heave	-0.615	-0.582
Longitudinal phugoid	0.097641 ± 0.25913	0.108 ± 0.2779
Yaw	-1.673	-0.718
Lateral phugoid	0.0017542 ± 0.22526	0.0015 ± 0.112

model as reported in [14]; 2) Rotor radius and UAV dimensions have been taken from SwissDrone SDO 50 V2 [30], since the superARTIS drone appears to be very similar; 3) Main rotors rotational speed Ω, inertial data, main rotor flapping spring constant K_β, blade moment of inertia I_β and blades characteristics data are those of the Yamaha R-50 helicopter [31], since superARTIS UAV is stated to be comparable to this Yamaha helicopter in [14]; 4) Fuselage and empennages parameters are scaled following the Froude scaling procedure detailed in [32], [33].

The adapted data have been used as input data in the synchropter model developed in this paper, then trimmed and finally linearized in hovering condition. Results are presented both in Fig. 20 and Table 2 for the case of synchropter hovering flight.

In Fig. 20 the poles of superARTIS synchropter are showed, in red the identified poles taken from [14] and in black those ones coming from the adapted model of this paper. Each mode is indicated in the figure with a different marker, illustrated in the legend. If compared to modes of the full-scale synchropter vehicle, the behaviour in hovering is quite similar. Roll and pitch subsidence (full and empty circles in Fig. 20) are stable modes, with roll subsidence being more stable than pitch, as well as heave and yaw (respectively with cross and rhombus markers). Longitudinal and lateral phugoid in Fig. 20 are both unstable oscillatory modes, as also reported for full-scale synchropter. Upon analyzing the comparison with data from identified superARTIS, it becomes evident that the heave, phugoid, and lateral phugoid modes are well captured by the scaled synchropter model developed in this study. These modes exhibit a strong correlation with the experimental data, suggesting that the overall dynamic behaviour of the vehicle in these aspects has been captured. However, significant discrepancies are observed in the roll and pitch subsidence modes, where the model slightly diverges from the identified data. This divergence may be attributed to the scaling methodology applied to the empennage surfaces. The altered scaling likely resulted in variations in the aerodynamic moments generated by these surfaces following a perturbation, leading to deviations in the vehicle's predicted roll and pitch dynamics. This suggests that further refinement of the empennage scaling procedure is necessary to improve the accuracy of the model in representing the vehicle's subsidence behaviour.

6. Conclusions

This paper develops a generic analytical model for the flight dynamics study of a synchropter helicopter configuration. This model is then trimmed and linearized in order to study the dynamic stability of the synchropter helicopter. The key findings of this research are listed:

- The trim results show that the synchropter yawing moment is naturally balanced for almost all forward speeds. In addition, the lack of a tail rotor as in a classical helicopter considerably minimizes the bank angle ϕ. Also, for a synchropter, a very minimal lateral cyclic control is needed across the speed range. This proves a strong advantage of the synchropter configuration as compared to a classical helicopter, since no much lateral-directional compensation is needed for the pilot.
- The synchropter's dynamic stability analysis highlights that, on the lateral axis, the main difference between a synchropter and a classical helicopter concerns the lateral phugoid mode, which exhibits to be unstable at all speeds.
- The comparison between the hovering modes of the scaled synchropter model and existing identified data of the superARTIS, shows that the proposed analytical model represents well the longitudinal and lateral phugoid modes while overpredicting the roll and pitch subsidences. Such differences are most likely due to the scaling procedure in obtaining the data for superARTIS's empennages.

Future research should consider direct comparisons of these findings with a wider set of experimental data, if possible.

CRediT authorship contribution statement

Giulia Bertolani: Writing – review & editing, Writing – original draft, Validation, Software, Methodology, Formal analysis, Data curation, Conceptualization. **Emanuele L. de Angelis:** Formal analysis, Conceptualization. **Fabrizio Giulietti:** Supervision, Project administration, Conceptualization. **Marilena D. Pavel:** Writing – review & editing, Supervision, Methodology, Data curation, Conceptualization.

Declaration of competing interest

The authors declare that they have no known competing financial interests or personal relationships that could have appeared to influence the work reported in this paper.

Appendix A. Relevant synchropter data

Table A.3
Relevant synchropter data.

Parameter	Symbol	Synch	BO105	Units
Vehicle data				
Mass	m	2200	2200	kg
Principal moments of inertia	I_x	1863	1433	kg m^2
Principal moments of inertia	I_y	4983	4973	kg m^2
Principal moments of inertia	I_z	4086.7	4099	kg m^2
Inertia products	I_{xy},	858	660	kg m^2
Stationline position of CG	STA_{CG}	2.1337	2.1337	m
Buttline position of CG.	BL_{CG}	0	0	m
Waterline position of CG.	WL_{CG}	1.52	1.52	m
Rotor data				
Stationline position of hub	STA_H	2.1337	2.1337	m
Buttline position of left hub	BL_H	0.25	-	m
Buttline position of right hub	BL_H	-0.25	-	m

(*continued on next page*)

Table A.3 (*continued*)

Parameter	Symbol	Synch	BO105	Units
Waterline position of hub	WL_H	3	3	m
Number of rotor blades	N_{blades}	2	4	
Nominal angular velocity	Ω_{nom}	423.9918	423.9918	RPM
Radius	R	4.91	4.91	m
Mean blade chord	$\bar{c}$	0.27	0.27	m
Flapping spring constant	K_β	113330	113330	Nm/rad
Pitch-flap coupling tangent of δ_3	K_1	0	0	
Hinge offset	ϵ	0	0	m
Blade Inertia moment	I_β	231.7	231.7	kg m^2
Blade profile lift curve slope	C_{l_α}	6.113	6.113	rad^{-1}
Blade twist angle	θ_{tw}	-0.14	-0.14	rad
Tip loss factor	B	0.96	0.96	
Precone angle	a_0	0	rad	
Solidity	σ	0.035	0.07	
Lateral shaft tilt	$\frac{\Gamma}{2}$	12.5	-	deg
Fuselage (Fus.)				
Stationline position of fus.	STA_{CG}	2.15	2.15	m
Buttline position of fus.	BL_{CG}	0	0	m
Waterline position of fus..	WL_{CG}	1.52	1.52	m
Fus. plan area	S_p	7.4263	7.4263	m^2
Fus. side area	S_s	5.2	5.2	m^2
Horizontal Stabilizer (HS)				
Stationline position of HS	STA_{HS}	6.6937	6.6937	m
Buttline position of HS	BL_{HS}	0	0	m
Waterline position of HS	WL_{HS}	2	2	m
HS incidence angle	i_{HS}	0.0698	0.0698	rad
HS area	s_{HS}	0.803	0.803	m^2
HS mean aerodynamic chord	C_{HS}	0.674	0.674	m
HS aspect ratio	AR_{HS}	2.635	2.635	
HS dynamic pressure ratio	η_{HS}	0.633	0.633	
Vertical fin (Vf)				
Stationline position of Vf	STA_{VF}	7.5497	7.5497	m
Buttline position of Vf	BL_{VF}	0	0	m
Waterline position of Vf	WL_{VF}	2.5	2.5	m
Vf incidence angle	i_{VF1}	-0.08116	-0.08116	rad
Vf area	s_{VF1}	0.805	0.805	m^2
Vf sweep angle	λ_{VF1}	0	0	rad
Vf dynamic pressure ratio	η_{VF1}	0.41	0.41	
Vf mean aerodynamic chord	C_{VF1}	0.5358	0.5358	m

Appendix B. State and control matrices

$$A = \begin{bmatrix} X_u & X_w - Q_e & X_q - W_e & A_{14} & X_v + R_e & X_p & 0 & X_r + V_e \\ Z_u + Q_e & Z_w & Z_q + U_e & A_{24} & Z_v + P_e & Z_p - V_e & A_{27} & Z_r \\ M_u & M_w & M_q & 0 & M_v & A_{36} & 0 & A_{38} \\ 0 & 0 & \cos\Theta_e & 0 & 0 & 0 & A_{47} & \sin\Theta_e \\ Y_u - R_e & Y_w + P_e & Y_q & A_{54} & Y_v & Y_p + W_e & A_{57} & Y_r - U_e \\ L'_u & L'_w & A_{63} & 0 & L'_v & A_{66} & 0 & A_{68} \\ 0 & 0 & \sin\phi_e \tan\Theta_e & A_{74} & 0 & 1 & 0 & \cos\phi_e \tan\Theta_e \\ N'_u & N'_w & A_{83} & 0 & N'_v & A_{86} & 0 & A_{88} \end{bmatrix}$$

where:

$A_{14} = -g\cos\Theta_e$, $A_{24} = -g\cos\phi_e\sin\Theta_e$, $A_{27} = -g\sin\phi_e\cos\Theta_e$, $A_{36} = M_p - 2P_eI_{xz}I_{yy} - R_e(I_{xx} - I_{zz})I_{yy}$, $A_{38} = M_r + 2R_eI_{xz}I_{yy} - P_e(I_{xx} - I_{zz})I_{yy}$, $A_{47} = -\Omega_a\cos\Theta_e$, $A_{54} = -g\sin\phi_e\sin\Theta_e$, $A_{57} = g\cos\phi_e\cos\Theta_e$, $A_{63} = L'_q + k_1P_e - k_2R_e$, $A_{66} = L'_p + k_1Q_e$, $A_{68} = L'_r - k_2Q_e$, $A_{74} = \Omega_a\sec\Theta_e$, $A_{83} = N'_q - k_1R_e - k_3P_e$, $A_{86} = N'_p - k_3Q_e$, $A_{88} = N'_r - k_1Q_e$.

A is the state matrix. B, the control matrix, is:

$$B = \begin{bmatrix} X_{\Theta_0} & X_{A_1} & X_{B_1} & X_{\Theta_{0T}} \\ Z_{\Theta_0} & Z_{A_1} & Z_{B_1} & Z_{\Theta_{0T}} \\ M_{\Theta_0} & M_{A_1} & M_{B_1} & M_{\Theta_{0T}} \\ 0 & 0 & 0 & 0 \\ Y_{\Theta_0} & Y_{A_1} & Y_{B_1} & Y_{\Theta_{0T}} \\ L'_{\Theta_0} & L'_{A_1} & L'_{B_1} & L'_{\Theta_{0T}} \\ 0 & 0 & 0 & 0 \\ N'_{\Theta_0} & N'_{A_1} & N'_{B_1} & N'_{\Theta_{0T}} \end{bmatrix}$$

The longitudinal and lateral state matrices are:

$$A_{LON} = \begin{bmatrix} X_u & g\cos\Theta_e/U_e & X_w - g\cos\Theta_e/U_e & X_q - W_e \\ Z_u & g\sin\Theta_e/U_e & Z_w - g\sin\Theta_e/U_e & Z_q \\ Z_u & g\sin\Theta_e/U_e & Z_w - g\sin\Theta_e/U_e & Z_q + U_e \\ M_u & 0 & M_w & M_q \end{bmatrix}$$

$$A_{LAT} = \begin{bmatrix} 0 & 0 & Y_v & g \\ 0 & 0 & 1 & 0 \\ -N'_r & -U_eN'_v & N'_r + Y_v & g - N'_pU_e \\ L'_r/U_e & L'_v & -L'_r/U_e & L'_p \end{bmatrix}$$

Data availability

Data will be made available on request.

References

[1] R. Ford, Germany's Secret Weapons of World War II, Amber Books, London, United Kingdom, 2000.

[2] Z. Gao, J. Li, X. Shao, L. Zeng, Numerical simulation and aerodynamic investigation of the intermeshing rotor in hover, J. Phys. Conf. Ser. 2252 (1) (2022), https://doi.org/10.1088/1742-6596/2252/1/012056.

[3] F. Wei, E. Moore, A. Gates, An intermeshing rotor helicopter design and test, in: AIAA SciTech 2015, Kissmmee, Florida, January 5-9, 2015.

[4] J.G. Leishman, Principles of Helicopter Aerodynamics, Cambridge University Press, 2000.

[5] E.G. Sweet, Hovering Measurements for Twin-Rotor Configurations with and Without Overlap, Langley Research Center, Langley Field, Va, Nov. 1960.

[6] M. Mansur, M. Tischler, M. Bielefield, J. Bacon, K. Cheung, M. Berrios, K. Rothman, Full flight envelope inner-loop control law development for the unmanned k-max, in: 67th American Helicopter Society Annual Forum, Virginia Beach, VA, May 3-5, 2011.

[7] C. Frost, M. Tischler, M. Bielefield, T. LaMontagne, Design and test of flight control laws for the kaman burro unmanned aerial vehicle, in: AIAA, Atmospheric Flight Mechanics Conference, Denver, CO, U.S.A., August 14-17, 2000.

[8] J. Colbourne, M. Tischler, C. Tomashofski, T. LaMontagne, System identification and control system design for the burro autonomous uav, in: Proceedings for the American Helicopter Society 56th Annual Forum, Virginia Beach, VA, May, 2000.

[9] J. McGonagle, The design, test and development challenges of converting the k-max® helicopter to a heavy lift rotary wing uav, in: Proceedings of the American Helicopter Society Annual Forum 57th, Washington, DC, May 9-11, 2001.

[10] Z.B. Saribay, F. Wei, C. Sahay, Optimization of an intermeshing rotor transmission system design, in: 46th AIAA/ASME/ASCE/AHS/ASC Structures, Structural Dynamics and Materials Conference, Austin, Texas, April 18-21, 2005.

[11] A. Barth, C. Spieb, K. Kondak, M. Hajek, Design, analysis and flight testing of a high altitude synchropter uav, in: AHS International 74th Annual Forum&Technology Display, Phoenix, Arizona, USA, May 14-17, 2018.

[12] A. Barth, R. Feil, K. Kondak, M. Hajek, Conceptual study for an autonomous rotorcraft for extreme altitudes, 2014.

[13] V. Zappek, I. Yavrucuk, Fuel cell sizing for a uav with intermeshing rotors using a genetic algorithm for ndarc rotor performance calibration, in: 79th Vertical Flight Society and Annual Forum & Technology Display, West Palm Beach, FL, USA, May 16-18, 2023.

[14] J. Wartmann, S. Seher-Weib, P. Petit, A. Dikarew, A. Voigt, K.K. Fettig, System identification of a compound intermeshing rotor uav, in: 79th Vertical Flight Society and Annual Forum & Technology Display, West Palm Beach, FL, USA, May 16-18, 2023.

[15] F.D. Harris, Twin rotor hover performance, J. Am. Helicopter Soc. 44 (1) (1999) 34–37, https://doi.org/10.4050/JAHS.44.34.

[16] B. Theys, G. Dimitriadis, P. Hendrick, J. De Schutter, Influence of propeller configuration on propulsion system efficiency of multi-rotor unmanned aerial vehicles, in: International Conference on Unmanned Aircraft Systems (ICUAS), 2016, pp. 195–201.

[17] J.F. Tan, T.Y. Zhou, Y.M. Sun, G.N. Barakos, Numerical simulation andof the aerodynamic interaction between a tiltrotor and a tandem rotor during shipboard operations, Aerosp. Sci. Technol. 87 (2019) 62–72, https://doi.org/10.1016/j.ast.2019.02.005.

[18] J.G. Leishman, M. Syal, Figure of merit definition for coaxial rotors, J. Am. Helicopter Soc. 53 (3) (July 2008) 290–300, https://doi.org/10.4050/JAHS.53.290.

[19] A. Bramwell, The longitudinal stability and control of the tandem-rotor helicopter - part I, aeronautical research council reports and memoranda, Rep. Memo. No 3223 (January 1960).

[20] A. Bramwell, The lateral stability and control of the tandem-rotor helicopter - part ii, aeronautical research council reports and memoranda, Rep. Memo. No 3223 (January 1960).

[21] W.Z. Stepniewski, Rotary-Wing Aerodynamics, Dover Publications, 1979.

[22] Y. Cao, G. Li, Q. Yang, Studies of trims, stability, controllability, and some flying qualities of a tandem rotor helicopter, Proc. Inst. Mech. Eng., G J. Aerosp. Eng. 223 (2) (2009) 171–177, https://doi.org/10.1243/09544100JAERO462.
[23] D.A. Peters, N. HaQuang, Dynamic inflow for practical applications, J. Am. Helicopter Soc. 33 (4) (1988) 64–68, https://doi.org/10.4050/JAHS.33.64.
[24] P.D. Talbot, B.E. Tinling, W.A. Decker, R.T.N. Chen, A Mathematical Model for a Single Main Rotor Helicopter for Piloted Simulation, Ames Research Center, Moffett, Field, California, Sept. 1982.
[25] G.D. Padfield, Helicopter Flight Dynamics, Blackwell Publishing, 1996.
[26] H.S. Choi, E.T. Kim, D.I. You, H. Shim, Improvements in small-scale helicopter rotor modeling for the real-time simulation of hovering flight, Jpn. Soc. Aeronaut. Space Sci. 54 (185/186) (2011) 229–237, https://doi.org/10.2322/tjsass.54.229.
[27] J.R. Dormand, Numerical Methods for Differential Equations: A Computational Approach, CRC Press, 1996.
[28] P.R. W., Helicopter Performance, Stability and Control, Krieger Publishing Company, Inc., 1989.
[29] R. van Aalst, M.D. Pavel, On the question of adequate modelling of steady-state rotor disc-tilt for helicopter manoeuvering flight, in: 28^{th} European Rotorcraft Forum, 17-20 September, Bristol, UK, 2002.
[30] Swissdrones, https://www.swissdrones.com.
[31] B. Mettler, Identification Modeling and Characteristics of Miniature Rotorcraft, Springer Science+Business Media, LLC, 2003.
[32] B. Mettler, C. Dever, E. Feron, Scaling effects and dynamic characteristics of miniature rotorcraft, J. Guid. Control Dyn. 27 (3) (2004), https://doi.org/10.2514/1.10336.
[33] B. Mettler, C. Dever, E. Feron, Identification modeling, flying qualities and dynamic scaling of miniature rotorcraft, in: NATO SCI-120 Symposium on Challenges in Dynamics, System Identification, Control and Handling Qualities for Land, Air, Sea and Space Vehicles, Berlin, Germany, May, 2002.